PERGAMON

International Journal of Solids and Structures 37 (2000) 3733–3760

INTERNATIONAL JOURNAL OF SOLIDS and STRUCTURES

www.elsevier.com/locate/ijsolstr

Three dimensional cohesive-element analysis and experiments of dynamic fracture in C300 steel

A. Pandolfi[a], P.R. Guduru[b], M. Ortiz[b,*], A.J. Rosakis[b]

[a]*Dipartimento di Ingegneria Strutturale, Politecnico di Milano, 20133, Milano, Italy*
[b]*Graduate Aeronautical Laboratories, California Institute of Technology, Mail Stop 105-50, Pasadena, CA 91125, USA*

Received 9 November 1998; in revised form 6 May 1999

Abstract

The dynamic drop-weight test is taken as a convenient basis for assessing the fidelity and predictive ability of cohesive models of fracture in applications involving dynamic crack growth. In the experimental phase of the study, coherent gradient sensing (CGS) has been used to study dynamic fracture in C300 maraging steel. The specimens were subjected to three-point bend impact loading under a drop weight tower. High-speed photographs of the CGS interferograms were analyzed to determine the crack tip location, the velocity and the dynamic fracture toughness as a function of time. Post-mortem examination of the specimens revealed the fractography of the fracture surfaces, including the development of shear lips. In a parallel numerical phase of the study, fracture has been modeled by recourse to an irreversible cohesive law embedded into cohesive elements. These cohesive elements govern all aspects of the separation and closure of the incipient cracks. The cohesive behavior of the material is assumed to be rate independent. The finite element model is three dimensional and consists of quadratic ten-noded tetrahedra. The numerical simulations have proven highly predictive of a number of observed features, including: the crack growth initiation time; the trajectory of the propagating crack tip; and the formation of shear lips near the lateral surfaces. The simulations therefore establish the feasibility of using cohesive models of fracture and cohesive elements to predict dynamic crack-growth initiation and propagation in three dimensions.

Keywords: Dynamic fracture; Coherent gradient sensing; 3D cohesive elements; C300 steel; Three point bend; Drop weight test

1. Introduction

When a mode I crack initiates dynamically, after the satisfaction of an appropriate dynamic crack

* Corresponding author. Fax: +1-626-304-0175.
E-mail address: ortiz@madrid.caltech.edu (M. Ortiz).

0020-7683/00/$ - see front matter
PII: S0020-7683(99)00155-9

initiation condition (Owen et al., 1998), it grows with a crack tip speed history not predictable by continuum mechanics alone. To describe the crack tip history, we require the notion of a dynamic crack growth toughness which would in general be a material-dependent function of a near tip measure of the local deformation rate. For growing cracks, the dominant contribution to the strain rate near the propagating crack tip is proportional to the instantaneous crack tip speed. As a result, the dynamic fracture toughness is expected to be some material-dependent function of the crack tip speed. These observations suggest a dynamic fracture criterion of the form (e.g. Freund, 1990):

$$K_{\mathrm{I}}^{\mathrm{d}}[a(t),\, t,\, \mathrm{load}] = K_{\mathrm{D}}(v) \tag{1}$$

where $a(t)$ is the time-dependent crack length and v is the crack velocity $\dot{a}(t)$. The left-hand side of this equation, namely, the instantaneous stress intensity factor $K_{\mathrm{I}}^{\mathrm{d}}$, measures the strength of the near-tip fields which drive crack propagation. The right-hand side of the equation, called the dynamic fracture toughness, K_{D}, represents the resistance of the material to crack propagation, with the attendant dissipative mechanisms, such as surface energy and plasticity, and material inertia subsumed within it. As implied in Eq. (1), K_{D} is generally supposed to be a function of the crack velocity v. Numerical analyses by Freund and Douglas (1982) and Lam and Freund (1984) have shown that, for elastic–plastic materials, material inertia shields the crack tip plasticity for a propagating crack. Correspondingly, for materials obeying McClintock and Irwin's (1964) fracture criterion, i.e. the attainment of a critical plastic strain at a fixed critical distance ahead of the crack tip, the aforementioned numerical analyses reveal that $K_{\mathrm{D}}(v)$ is an *increasing* function of v, in keeping with experimental observation. Rosakis and Zehnder (1985) have shown that this type of analyses are predictive of the variation of K_{D} with v for appropriately assumed values of certain parameters.

Over the past two decades, considerable experimental effort — using a variety of techniques — has been devoted to the development of methods to measure $K_{\mathrm{D}}(v)$, and to ascertaining if it indeed is a material property. In addition to direct optical techniques such as the method of caustics, photoelasticity and coherent gradient sensing (CGS), certain hybrid methods have also been used for this purpose. Brickstad (1983) conducted dynamic fracture experiments on a high strength steel where the crack velocity and boundary displacements were experimentally measured and were used as input to a numerical analysis to infer the variation of $K_{\mathrm{D}}(v)$. A significant result of this work is that $K_{\mathrm{D}}(v)$ does not show a discernible dependence on $\dot{v}$, i.e. the crack acceleration, which is consistent with experimental observations (Dally, 1979). Employing an analogous procedure, Kanazawa et al. (1981) obtained an extensive set of data concerning $K_{\mathrm{D}}(v)$ at various test temperatures for a Si–Mn steel. In addition, taking advantage of the large size of the specimens, they made use of the data to predict v vs a for a given boundary loading. The results are in good agreement with experiments. In their procedure, they made use of Freund's (1972) decomposition of $K_{\mathrm{I}}^{\mathrm{d}}(a,\, v)$ into a product of functions of a and v alone.

A similar approach was adopted by Angelino (1978) who inferred K_{D} from boundary load and displacement measurements. Though prone to errors in crack-velocity estimation, this method yielded K_{D} values for SAE 4340 steel that are in good agreement with those reported by other investigators. A slightly different methodology was adopted by Bilek (1980), who subjected double cantilever beam (DCB) specimens made of 4340 steel to wedge loading and measured crack speed and boundary displacements. This information was used in the numerical solution of an analytical model in which the DCB specimen was modeled as a Timoshenko beam on a rigid foundation. His results suggest that K_{D} goes through a minimum before rapidly rising as a function of v. The issue of K_{D} going through a minimum at a nonzero velocity is of great significance in crack arrest considerations. Given the inaccuracies in the measurement of crack velocity and the limitations in the interpretation of the experimental results, this question invites further experimental studies with improved accuracy. From

the theoretical point of view, this phenomenon has been recently linked to material rate sensitivity by the work of Freund and Hutchinson (1985) and Freund et al. (1986).

Despite these advances, the dynamic fracture criterion (1) should not be construed as a universal relation, and the assumptions implicit in such criteria, which determine their scope and range of applicability, should be carefully noted. Firstly, since (1) is written in terms of stress-intensity factors, the small-scale yielding condition of linear-elastic fracture mechanics (LEFM) is tacitly assumed to be in force. For this assumption to be appropriate, the plastic zone must be confined to a region near the tip of the crack much smaller that any and all remaining geometrical dimensions of the problem, including the crack length, ligament size, and others. Secondly, a statement of the form (1) tacitly presumes that the asymptotic near-tip fields, including plastic deformations and inertia, are autonomous, with their form independent of the shape and size of the crack, the geometry of the body, the loading configuration and the load history. Under these conditions, the near-tip fields which mediate the separation processes are fully characterized by a limited set of parameters, e.g. the stress-intensity factors, and it is reasonable to assume that the crack-tip motion is a function of these parameters only. In effect, the principal objective behind the dynamic fracture criterion (1) is to conveniently encapsulate a vast array of micromechanical processes attendant to a moving crack tip, such as plasticity, inertia, heat conduction and others, so that such phenomena need not be explicitly accounted for in full-system analyses.

In many cases, however, it may be unreasonable to expect that such complex interacting processes as accompany a running crack may be subsumed within as simple a relation as (1). For instance, the fracture criterion (1) may be expected to break down under fully yielded conditions, or near a free surface owing to the emergence of shear lips. In the work presented in this paper, we have endeavored to validate an entirely different approach based on:

1. *Multiscale analysis*. Advances in adaptive mesh refinement and other computational methods presently enable the simultaneous resolution of full-system fields as well as near-tip fields, with the result that the latter need not be accounted for, i.e. buried, in the fracture criterion.
2. *Cohesive theories of fracture*. The explicit resolution of the near-tip fields has the far-reaching consequence that only the actual surface-separation processes need to be contemplated in the fracture criterion. Here, those separation processes are modeled by recourse to cohesive theories of fracture and their computational embodiment, cohesive elements.

In the present work, we take the dynamic drop-weight test as a convenient basis for assessing the predictive ability of cohesive models of fracture in applications involving dynamic crack growth. These models — pioneered by Dugdale (1960), Barrenblatt (1962), Rice (1968) and others — regard fracture as a gradual phenomenon in which separation takes place across an extended crack 'tip', or cohesive zone, and is resisted by cohesive tractions. Cohesive models enable the incorporation into the analysis of bona fide fracture parameters such as the spall strength — the peak cohesive traction — and the fracture energy — the area under the cohesive law — of the material. In particular, the existence of a well-defined fracture energy endows the solid with characteristic, or 'intrinsic', spatial and temporal lengthscales. The particular class of cohesive law contemplated in the present work is due to Ortiz and Pandolfi (1999) and accounts for finite kinematics and irreversible behavior. Other alternative formulations may be found elsewhere (Rose et al., 1981; Needleman, 1987; Ortiz, 1988; Beltz and Rice, 1991; Rice, 1992; Ortiz and Suresh, 1993).

Cohesive laws have been built into finite element analyses as mixed boundary conditions (Hillerborg et al., 1976; Carpinteri, 1986; Needleman, 1987, 1990a, b, 1992; Xu and Needleman, 1993; Planas et al., 1994; Tvergaard and Hutchinson, 1993, 1996a, b) or have been embedded into *cohesive finite elements* (Willam, 1989; Ortiz and Suresh, 1993; Camacho and Ortiz, 1997; Xu and Needleman, 1994, 1995, 1996; De-Andrés et al., 1998; Ortiz and Pandolfi, 1999). These elements are surface-like and are compatible

with general bulk finite element discretizations of the solid, including those which account for dynamics, plasticity and large deformations. Cohesive elements bridge nascent surfaces and govern their separation in accordance with a cohesive law. In two-dimensional fragmentation simulations, both plane strain and axisymmetric, Camacho and Ortiz (1996) and Ortiz (1996) have established the feasibility of using cohesive elements to account explicitly for individual cracks as they nucleate, propagate, branch and possibly link up to form fragments, as well as of simulating explicitly the granular flow which ensues following widespread fragmentation. Camacho and Ortiz (1996) have also shown that mesh-size independent results are obtained when the mesh adequately resolves the cohesive zone. The fidelity of cohesive elements in applications involving dynamic fracture in ductile materials has recently been investigated by Pandolfi et al. (1999), who have simulated the expanding 1100-0 aluminum ring test of Grady and Benson (1983). The numerical simulations have been found to be highly predictive of a number of observed features, including: the number of dominant and arrested necks; the fragmentation patterns; the dependence of the number of fragments and the fracture strain on the expansion speed; and the distribution of fragment sizes at fixed expansion speed.

The organization of the paper is as follows. The test configuration and diagnostic techniques employed in the experimental phase of this study are briefly discussed in section 2, which also collects the observational data and their analysis. The particulars of the cohesive laws and elements adopted in the numerical phase of the study are succinctly summarized in section 3. Detailed comparisons between full three-dimensional finite-element simulations and the experimental data are presented in section 4. These comparisons demonstrate that cohesive theories accurately predict sensitive aspects of the dynamic fracture of C300 steel such as crack-growth initiation conditions and crack propagation velocities.

2. Dynamic fracture of C300 steel

A common approach in dynamic fracture testing is to observe the propagating crack tip area using an optical technique and to infer the K_I^d value. These methods rely upon an accurate analytical description of the near crack tip stress fields. A number of analytical crack-tip fields are presently available giving the dominant singular term as well as higher-order expansions for many problems, including steady-state crack propagation and transient crack propagation. Some of the experimental methods presently in use are caustics, photoelasticity and CGS. Early attempts at using the method of caustics for propagating cracks were made by Kalthoff et al. (1976), Katsamanis et al. (1977), Theocaris (1978) and Goldsmith and Katsamanis (1979). They used quasi-static crack-tip fields for analyzing the dynamic shadow patterns, neglecting inertial effects. As the crack velocity becomes a substantial fraction of the Rayleigh wave speed, the inertial effects significantly modify the crack tip stress fields. Kalthoff *et al.* (1978) introduced an approximate correction factor to be applied to static analysis to account for dynamic effects. The first accurate, fully dynamic analysis of caustics was carried out by Rosakis (1980). However, this analysis was based on the assumption of steady state crack growth. Later Beinert and Kalthoff (1981), Rosakis et al. (1984, 1988), Ravi-Chandar and Knauss (1983, 1984a, b, c, d), Kalthoff (1985), Zehnder and Rosakis (1986, 1990) and Knauss and Ravi-Chandar (1985) used this fully dynamic analysis in the interpretation of their experimental data.

These analyses assume the existence of a region of K_I^d dominance near the crack tip. The question of K_I^d-dominance around a propagating crack tip was addressed in detail by Krishnaswamy and Rosakis (1990). Their results suggest that the value of K_D obtained using steady-state analyses could be in error by as much as 30% in the presence of transient effects. Following the development of solutions for transient crack propagation by Freund and Rosakis (1992), Liu et al. (1993) discussed a consistent way to analyze caustic patterns generated in the presence of transient effects. This procedure is yet to be

Ni	Co	Mo	Ti	Si	Al
18.1	9.1	4.95	0.65	0.08	0.05

Fig. 1. Chemical composition of C300 maraging steel.

applied to actual experimental data. Despite being attractive for its simplicity, the method of caustics needs to be evaluated carefully for its use in transient crack propagation.

Dynamic photoelasticity has been extensively used for crack propagation problems by many investigators on birefringent polymers and later adopted to metals. This technique has been discussed in great detail by Kobayashi (1978), Irwin et al. (1979) and Kobayashi and Dally (1980). Irwin (1958) and Bradley and Kobayashi (1970) used a two parameter approach to extract fracture parameters from the photoelastic fringes by a single point measurement. Further improvements in fringe analysis were made by Sanford and Dally (1979) who used a three-parameter approach and a least-squares procedure to analyze data from many fringes. Being a full field technique, photoelasticity gives information about the stress field in a finite area around the crack tip. As the distance from the crack tip increases, the higher-order terms become significant and must be accounted for. A higher-order asymptotic expansion given by Atluri and Nishioka (1983) for a steadily propagating crack was used by Dally et al. (1985), Chona et al. (1983), Chona and Sanford (1988), Sanford and Chona (1984) and Shukla and Chona (1988) to obtain dynamic fracture toughness. But, as pointed out by Rosakis (1993) and Krishnaswamy and Rosakis (1990), the relative importance of the higher-order terms in transient crack propagation is influenced not only by the distance from the crack tip, but also by the time histories of the crack propagation velocity and the stress intensity factor. Thus, though the steady-state higher-order analysis of photoelastic fringes is an improvement over the previous methods, it might still be inadequate in obtaining accurate fracture parameters. In addition, application of photoelasticity to metals requires the use of birefringent coatings and other techniques which could themselves introduce errors.

Another full-field technique that has been in use in recent years is the method of CGS (Rosakis, 1993). This technique is readily applicable to transparent as well as opaque materials in addition to being insensitive to rigid-body motions of the specimen. Initial studies of the applicability of CGS to dynamic crack propagation were conducted by Krishnaswamy et al. (1992) on PMMA. The fringes were analyzed using the transient elastodynamic field. The results of their study demonstrated that the stresses and strains around a propagating crack could be described with good accuracy by the transient field mentioned above, and that the fracture parameters could be extracted reliably from the analysis. In addition, for transient dynamic fracture studies, where the interpretation of caustics has been questioned (Rosakis, 1993) dynamic CGS has enabled the investigation of causes that lead to problems with caustics. Caustics by reflection has so far been the dominant optical method applied to study dynamic crack growth in opaque structural materials. The ability of CGS to investigate dynamic fracture problems in opaque materials makes this full-field technique an attractive alternative to caustics. In the present investigation, CGS has been used to study dynamic fracture in C300 maraging steel (Fig. 1). The details of the optical technique and experimental setup are succinctly summarized next.

2.1. Optical technique and experimental setup

The optical technique of CGS is a shearing interferometric technique that is sensitive to inplane gradients of out of plane displacements in reflection mode and in-plane stress gradients in transmission mode. This technique can be thought of as the full field equivalent of the optical method of caustics. Detailed description of the technique, the equations governing optical mapping and fringe formation can

be found in Tippur et al. (1990, 1991) and in Rosakis (1993). A schematic illustration of the experimental setup along with the optical technique is shown in Fig. 2. For opaque materials, this technique involves reflecting a collimated laser beam from the surface of the deforming specimen and optically shearing it by sending it through two high density gratings separated by a distance Δ. This gives rise to multiple diffraction spots of orders 0, ± 1, ± 2, ... and the interference fringe pattern given by the $+1$ or the -1 order spot was recorded by the imaging system. In the current experiments, the beam has been sheared in a direction along the crack. The governing equation for interpreting the interference fringes is:

$$u_{3,\,1} = \frac{\partial u_3}{\partial x_1} = \frac{mp}{2\Delta} \tag{2}$$

where u_3 is the out of plane displacement of the specimen surface, x_1 is the direction of shearing of beam, m is the fringe order and p is the pitch of the gratings. Thus, each fringe represents the locus of constant $u_{3,1}$ on the specimen surface.

The specimens were subjected to three point bend impact loading under a drop weight tower. The mass of the falling weight was 200 kg and the impact velocities ranged from 5 to 10 m/s. The specimens were made of C300 maraging steel, the chemical composition of which is shown in Fig. 1. They were cut from a 6.35 mm thick plate in annealed condition and a notch of 250 μm width was cut using electric discharge machining. The heat treatment involved aging them for 5 h at 482°C followed by air cooling. The specimens were then subjected to fatigue loading to grow a 1.5 mm long sharp crack. The surface of the specimen was then prepared by lapping and polishing to get high optical reflectivity.

During the experiment, a strain gage attached to the specimen at the impact location triggers a pulsing laser system upon impact. The pulsing system used was an argon ion laser of wavelength 514.5 nm and the pulse width was 8 ns. The laser system gives 80 distinct pulses at predetermined repetition rate and these pulses are reflected from the specimen surface. The reflected pulses, after passing through the CGS optics, are recorded using a high speed camera (Cordin 330A) capable of recording at a rate of 2 million frames per second. In the current experiments, the camera was operated at 0.24 million frames per second.

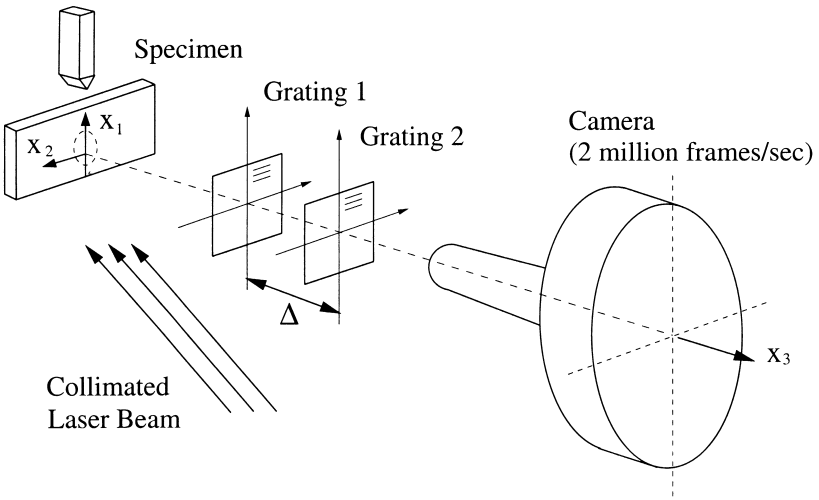

Fig. 2. Experimental setup for the drop weight test.

2.2. Experimental results and analysis

A typical sequence of high speed photographs of the CGS interferograms associated with propagating crack is shown in Fig. 3.

One could notice the stress waves associated with crack propagation indicating the transient nature of the process. From these pictures, the crack tip location as a function of time is measured. Using a three point polynomial fit, crack tip location is differentiated to get the crack velocity history. Fig. 16 shows the crack tip location history (Fig. 16(a), dark line) and the crack propagation velocity (Fig. 16(b), dark line) history for one experiment where the impact velocity was 10 m/s. In this experiment, crack propagation began 100 μs after impact. Freund and Rosakis (1992) and Rosakis et al. (1991) have developed a higher order description of the transient stress deformation state at the vicinity of a dynamically propagating crack. By recalling that the out of plane displacement field u_3 is proportional to the first stress invariant in-plane stress (i.e. $u_3 = -\nu/E(\sigma_{11} + \sigma_{22})$) and by using the appropriate transient higher order spatial description for the near tip stress field, one could rewrite equation (2) as follows:

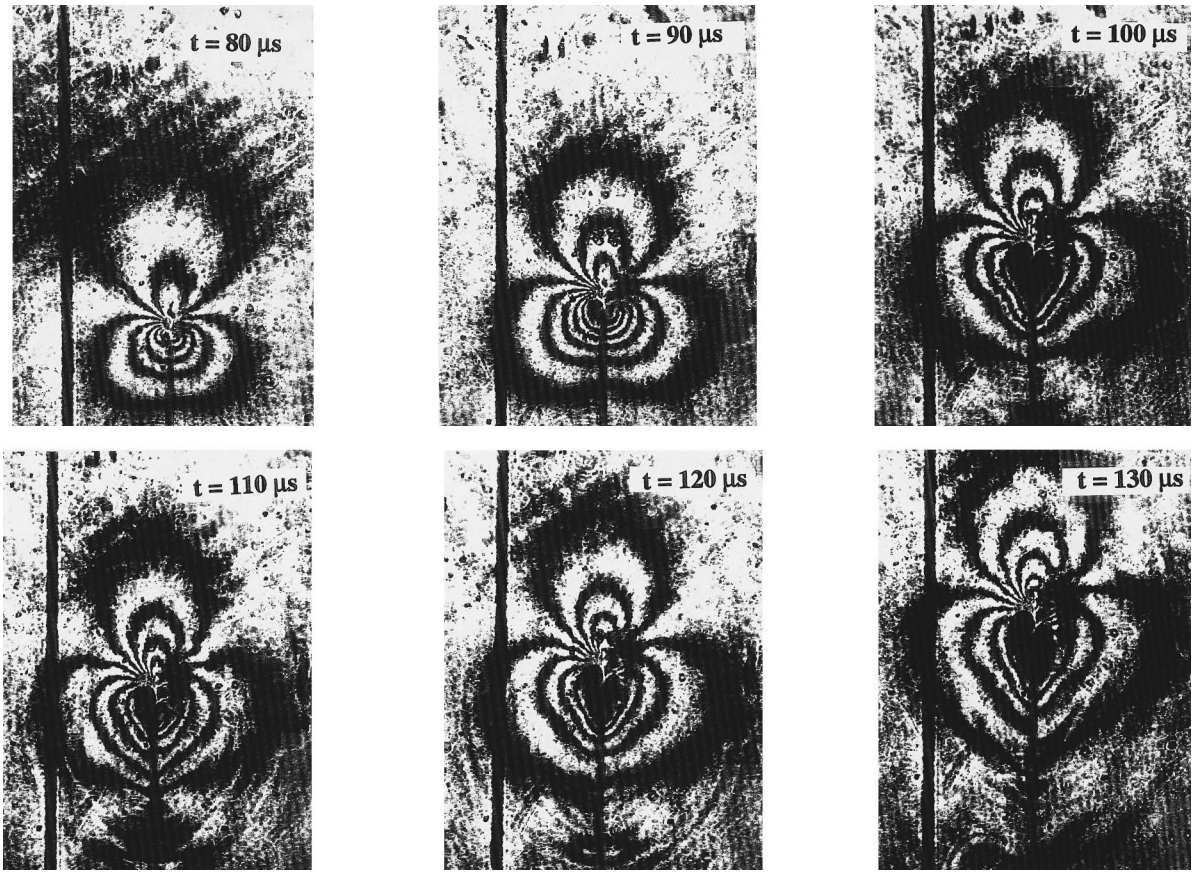

Fig. 3. Sequence of high speed photographs of the CGS interferograms. The time interval between the pictures is 10 μs. The first photograph refers 80 μs after the impact.

$$\left(\frac{mp}{2\Delta}\right)\frac{1}{D(v)}\,\frac{2E\sqrt{2\pi}}{vh}\,\frac{r_1^{3/2}}{\cos\,\phi_3} = K_{\mathrm{I}}^{\mathrm{d}} + \left[\beta_2\frac{\cos\,\phi_2}{\cos\,\phi_3} + \beta_3\frac{\cos\,\phi_5}{\cos\,\phi_3}\right]r_1 + \left[\beta_4\frac{1}{\cos\,\phi_3}\right]r_1^{3/2} + \left[\beta_5\frac{\cos\,\phi_2}{\cos\,\phi_3} + \beta_6 + \beta_7\frac{\cos\,\phi_7}{\cos\,\phi_3}\right]r_1^2 + \left[\beta_8\frac{\cos\,\phi_1}{\cos\,\phi_3}\right]r_1^{5/2} + O(r^3) \tag{3}$$

where

$$\phi_1 = \tan^{-1}(\alpha_1\,\tan\,\phi), \quad r_1 = r\,\cos\,\phi(1+\alpha_1\,\tan^2\phi) \tag{4}$$

$$\phi_2 = \frac{1}{2}\phi_1, \quad \phi_3 = \frac{3}{2}\phi_1, \quad \phi_5 = \frac{5}{2}\phi_1, \quad \phi_7 = \frac{7}{2}\phi_1 \tag{5}$$

$$D(v) = \frac{(1+\alpha_{\mathrm{s}}^2)(\alpha_{\mathrm{l}}^2-\alpha_{\mathrm{s}}^2)}{4\alpha_{\mathrm{l}}\alpha_{\mathrm{s}}-(1+\alpha_{\mathrm{s}}^2)^2}, \quad \alpha_{\mathrm{m}} = \left[1-\left(\frac{v}{c_{\mathrm{m}}}\right)^2\right]^{1/2} \quad (m = l,\, s) \tag{6}$$

c_{l} and c_{s} are the longitudinal and shear wave speeds, respectively, v is the Poisson's ratio, h is the specimen thickness and E is the Young's modulus. The polar coordinates r and ϕ are defined in Fig. 4. On the right hand side of the equation, $K_{\mathrm{I}}^{\mathrm{d}}$ is the dynamic stress intensity factor which is in general a function of time. $\beta_2 \ldots \beta_8$ are spatial constants which are also functions of time to be determined along with $K_{\mathrm{I}}^{\mathrm{d}}$. Let the left hand side of the above equation be denoted by $Z_{\mathrm{I}}^{\mathrm{d}}$ and the right hand side be denoted by $G_{\mathrm{I}}^{\mathrm{d}}(r,\,\phi;\,K_{\mathrm{I}}^{\mathrm{d}},\,\beta_2,\,\ldots,\,\beta_8)$. If $K_{\mathrm{I}}^{\mathrm{d}}$ dominance exists, $Z_{\mathrm{I}}^{\mathrm{d}}$ would be a constant and be equal to the instantaneous stress intensity factor $K_{\mathrm{I}}^{\mathrm{d}}$. If significant higher order terms exist, then the variation of $Z_{\mathrm{I}}^{\mathrm{d}}$ would be given by $G_{\mathrm{I}}^{\mathrm{d}}$ and the value of the stress intensity factor is obtained by setting $r = 0$ in $G_{\mathrm{I}}^{\mathrm{d}}$.

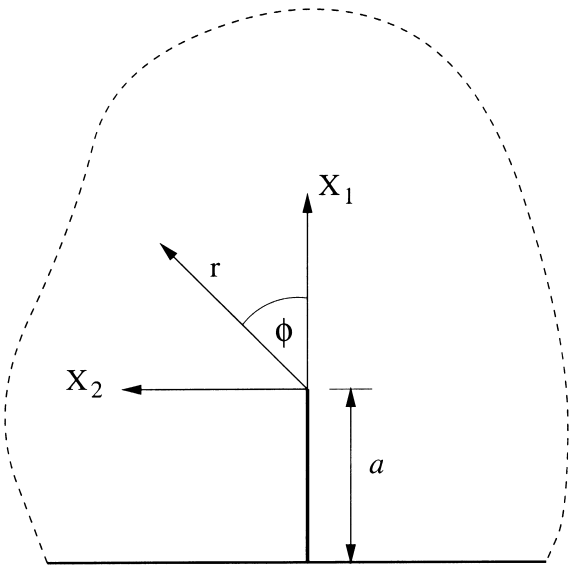

Fig. 4. Polar coordinate system referred in Eq. (4).

A least-squares procedure analogous to the one described by Tippur et al. (1991) was used to fit the above function $G_{\mathrm{I}}^{\mathrm{d}}$ to the experimental function $Z_{\mathrm{I}}^{\mathrm{d}}$ obtained from the CGS interferograms to extract $K_{\mathrm{I}}^{\mathrm{d}}$ and the β's. Since the above equations strictly hold for plane stress elastodynamics, one should be concerned about the sizes of the near tip three dimensional region (Rosakis and Ravi-Chandar, 1986) and the crack tip plastic zone. For the given material properties, the plastic zone size estimate was much smaller compared to the specimen thickness, leaving one to deal with the near tip three dimensional region whose radius is approximately equal to one half of the plate thickness (Rosakis and Ravi-Chandar, 1986). This has been taken care of by excluding any fringe data from the near tip three dimensional region in the analysis. This was done using the results from a three dimensional elastodynamic finite element analysis described by Krishnaswamy et al. (1991). Fig. 5 shows the results of one such analysis. In Fig. 5(a) the isolated points represent $Z_{\mathrm{I}}^{\mathrm{d}}$ obtained from experimental fringes and the dotted lines represent the constructed function $G_{\mathrm{I}}^{\mathrm{d}}$ from the least squares analysis. One could notice the good agreement along different radial directions. This could also be seen in the agreement between the digitized data points and the generated fringes using the parameters obtained from the least square procedure in Fig. 5(b), which demonstrates the applicability of dynamic CGS in conjunction with transient elastodynamic crack tip fields to measure fracture parameters. Fig. 6(a) shows the time history of the crack velocity and the time history of $K_{\mathrm{I}}^{\mathrm{d}}$ for one experiment where the impact velocity was 10 m/s. For a growing crack, a cross plot between these two time histories establishes the dependence of the critical value of the dynamic stress intensity factor (dynamic toughness K_{D}) on crack tip speed. K_{D} vs v data obtained from many different experiments is shown in Fig. 6(b). As is evident from the figure, the dynamic fracture toughness increases almost by a factor of two as the crack tip speed approaches 25–30% of the material Rayleigh wave speed. In Fig. 19(a), the fracture surface obtained in a 10 m/s impact velocity experiment is shown. One can notice that this surface is predominantly flat with small 45° shear lips at the edges.

3. Finite element model

We begin by considering the general case of a deformable body occupying an initial configuration $B_0 \subset R^3$. The boundary ∂B_0 of the body is partitioned into a displacement boundary $\partial B_{0,1}$ and a traction boundary $\partial B_{0,2}$. The body undergoes a motion described by a deformation mapping $\boldsymbol{\varphi}: B_0 \times [0, T] \rightarrow R^3$, where $[0, T]$ is the duration of the motion, under the action of body forces $\rho_0 \mathbf{b}$ and prescribed boundary tractions $\bar{\mathbf{t}}$ applied over $\partial B_{0,2}$. Let $\mathbf{F}$ be the attendant deformation gradients and $\mathbf{P}$ the first Piola–Kirchhoff stress tensor (cf, e.g. Marsden and Hughes, 1983). In addition, the solid contains a collection of cohesive cracks. The locus of these cracks on the undeformed configuration is denoted S_0, Fig. 7.

Under these conditions, the weak form of linear momentum balance, or virtual work expression, takes the form:

$$\int_{B_0} [\rho_0(\mathbf{b} - \ddot{\boldsymbol{\varphi}}) \cdot \boldsymbol{\eta} - \mathbf{P} \cdot \nabla_0 \boldsymbol{\eta}] \, \mathrm{d}V_0 - \int_{S_0} \mathbf{t} \cdot [\![\boldsymbol{\eta}]\!] \, \mathrm{d}S_0 + \int_{\partial B_{0,2}} \bar{\mathbf{t}} \cdot \boldsymbol{\eta} \, \mathrm{d}S_0 = 0 \tag{7}$$

where a superposed dot denotes the material time derivative, ∇_0 is the material gradient, $\boldsymbol{\eta}$ is an arbitrary virtual displacement satisfying homogeneous boundary conditions on $\partial B_{0,1}$, $\mathbf{t}$ are the cohesive traction over S_0, and $[\![\cdot]\!]$ denotes the jump across an oriented surface.

As is evident from (7), the presence of a cohesive surface results in the addition of a new term to the virtual work expression. Evidently, in order to complete the definition of the problem, a set of constitutive relations for the cohesive tractions $\mathbf{t}$ must be provided. These constitutive relations are in addition to and are independent of the conventional constitutive relations describing the bulk behavior

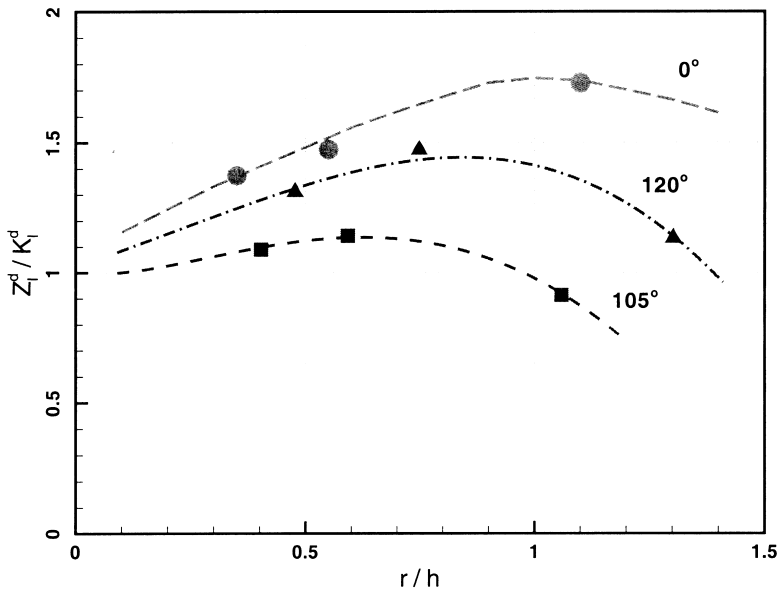

(a)

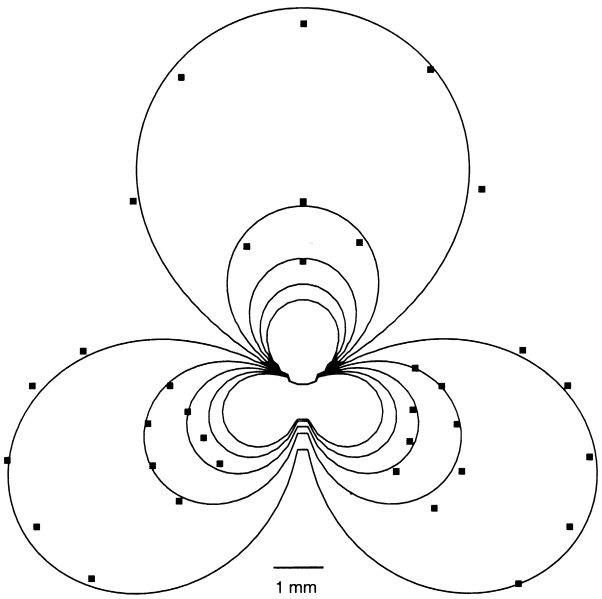

(b)

Fig. 5. (a) Least squares fitting procedure of the dominant near crack tip stress field. The isolated points represent Z_I^d obtained from experimental fringes and the lines represent the function G_I^d. (b) Comparison of the digitized experimental fringes (squares) and the theoretical generated fringes (lines).

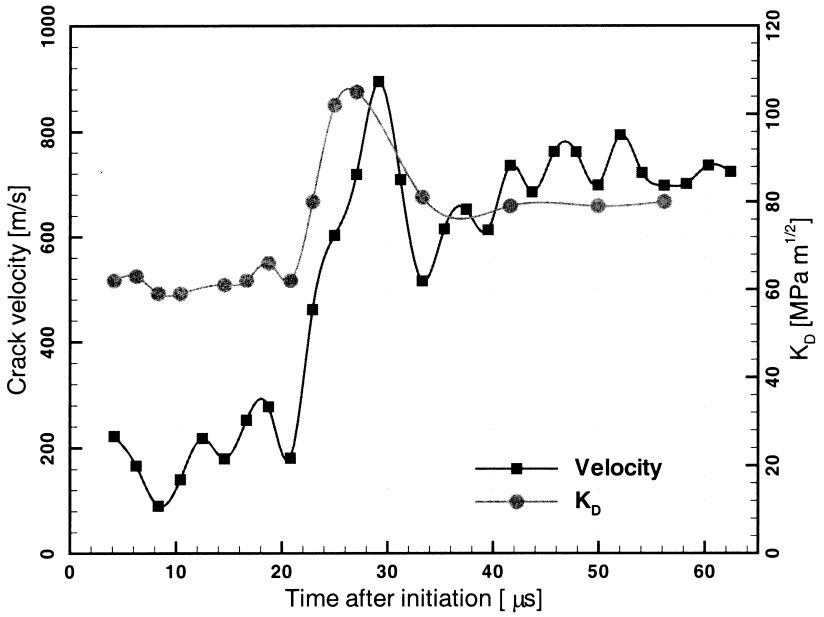

(a)

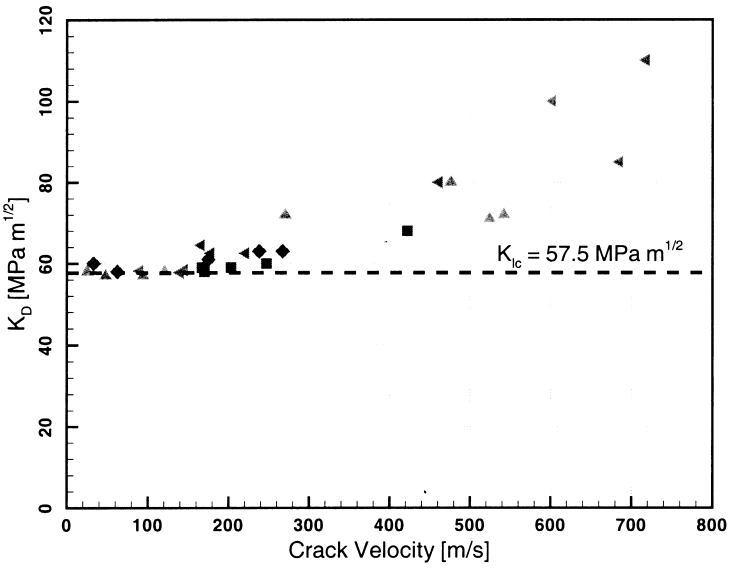

(b)

Fig. 6. (a) Time history of the crack tip velocity (squares) and K_D (circles); (b) Croos plot of K_D vs v for different experiments.

of the material. To this end, we postulate the existence of a free energy density per unit underformed area over S_0 of the general form

$$\phi = \phi(\boldsymbol{\delta}, \theta, \mathbf{q}; \mathbf{n}) \tag{8}$$

where

$$\boldsymbol{\delta} = [\![\boldsymbol{\varphi}]\!] \tag{9}$$

are the opening displacements over the cohesive surface, θ is the local temperature, $\mathbf{q}$ is some suitable collection of internal variables which describe the inelastic processes attendant to decohesion, and $\mathbf{n}$ is the unit normal to the cohesive surface in the deformed configuration. The explicit dependence of ϕ on $\mathbf{n}$ is required to allow for differences in cohesive behavior for opening and sliding. By recourse to Coleman and Noll's method (e.g. Lubliner, 1972, 1973) it is possible to show that the cohesive law takes the form

$$\mathbf{t} = \frac{\partial \phi}{\partial \boldsymbol{\delta}}. \tag{10}$$

The potential structure of the cohesive law is a consequence of the first and second laws of thermodynamics. The evolution of the internal variables $\mathbf{q}$ is governed by a set of kinetic relations of the general form

$$\dot{\mathbf{q}} = \mathbf{f}(\boldsymbol{\delta}, \theta, \mathbf{q}). \tag{11}$$

A more general class of free energies which allows for surface anisotropy and finite opening displacements have been considered by Ortiz and Pandolfi (1999).

To further simplify the formulation of mixed-mode cohesive laws, we follow Camacho and Ortiz (1996) and introduce an effective opening displacement

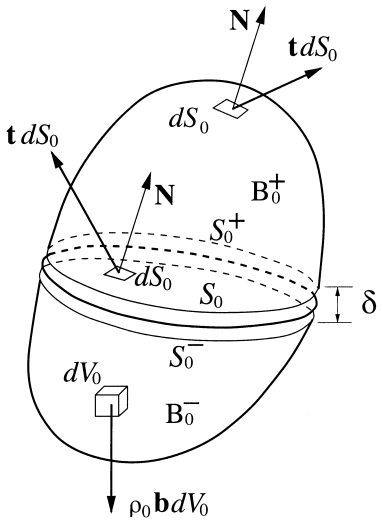

Fig. 7. Cohesive surface traversing a 3D body.

$$\delta = \sqrt{\beta^2 \delta_{\mathrm{S}}^2 + \delta_{\mathrm{n}}^2} \tag{12}$$

where

$$\delta_{\mathrm{n}} = \boldsymbol{\delta} \cdot \mathbf{n} \tag{13}$$

is the normal opening displacement and

$$\delta_{\mathrm{S}} = | \boldsymbol{\delta}_{\mathrm{S}} | = | \boldsymbol{\delta} - \delta_{\mathrm{n}} \mathbf{n} | \tag{14}$$

is the magnitude of the sliding displacement. Evidently, the parameter β assigns different weights to the sliding and normal opening displacements. A simple model of cohesion is then obtained by assuming that free energy potential ϕ depends on $\boldsymbol{\delta}$ only through the effective opening displacement δ, i.e.

$$\phi = \phi(\delta, \theta, \mathbf{q}). \tag{15}$$

Under these conditions, the cohesive law (10) reduces to

$$\mathbf{t} = \frac{t}{\delta}(\beta^2 \boldsymbol{\delta}_{\mathrm{S}} + \delta_{\mathrm{n}} \mathbf{n}) \tag{16}$$

where

$$t = \frac{\partial \phi}{\partial \delta}(\delta, \theta, \mathbf{q}) \tag{17}$$

is a scalar effective traction. It follows from (12) and (16) that the effective traction is

$$t = \sqrt{\beta^{-2} | \mathbf{t}_{\mathrm{S}} |^2 + t_{\mathrm{n}}^2}. \tag{18}$$

This relation shows that β defines the ratio between the shear and the normal critical tractions. In brittle

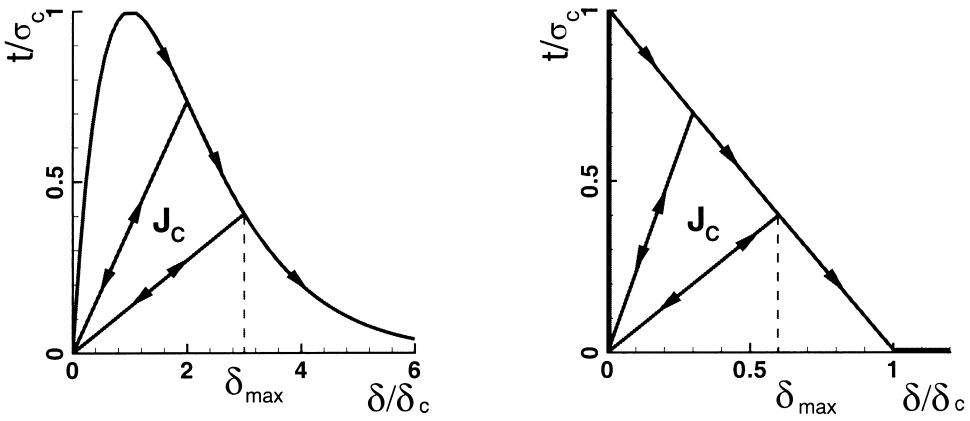

Fig. 8. Two simple choices of cohesive law, expressed in terms of an effective opening displacement δ and traction t: (a) loading-unloading rule from Smith–Ferrante envelop; (b) loading-unloading rule from linearly decreasing loading envelop.

materials, this ratio may be estimated by imposing lateral confinement on specimens subjected to high-strain-rate axial compression (Chen and Ravichandran, 1994, 1996). Upon closure, the cohesive surfaces are subject to the contact unilateral constraint, including friction. Since the dropweight experimental geometry of interest here does not lead to significant mode II sliding of the crack, we simply model crack closure in the spirit of penalty methods, i.e. by the introduction of a small surface compliance.

Fig. 8 depicts the particular type of irreversible cohesive laws envisioned here. Irreversibility manifests itself upon unloading. Therefore, an appropriate choice of internal variable is the maximum attained effective opening displacement $\delta_{\max}$. Loading is then characterized by the conditions: $\delta = \delta_{\max}$ and $\dot{\delta} \geq 0$. Conversely, we shall say that the cohesive surface undergoes unloading when it does not undergo loading. We assume the existence of a loading envelop defining a relation between t and δ under conditions of loading. A simple and convenient relation is furnished by Smith and Ferrante's universal binding law, Fig. 8(a), or by the linearly decreasing envelop shown in Fig. 8(b). Following Camacho and Ortiz (1996) we shall assume unloading to the origin, Fig. 8, giving

$$t = \frac{t_{\max}}{\delta_{\max}}\delta, \quad \text{if} \quad \delta < \delta_{\max} \ \text{ or } \dot{\delta} < 0. \tag{19}$$

For the present model, the kinetic relations (11) reduce to a straightforward computation of $\delta_{\max}$. In order to measure the extent of decohesion, we shall find it convenient to introduce a damage parameter

$$D = \frac{\phi(\delta_{\max})}{G_c}. \tag{20}$$

Evidently, D ranges from 0 to 1, with these limits corresponding to an uncracked solid and a fully formed new surface, respectively. Furthermore, we require that

$$\dot{D} \geq 0 \tag{21}$$

as befits the irreversibility of damage.

A particularly appealing aspect of cohesive laws as models of fracture is that they fit naturally within the conventional framework of finite element analysis. One possible approach is to implement the

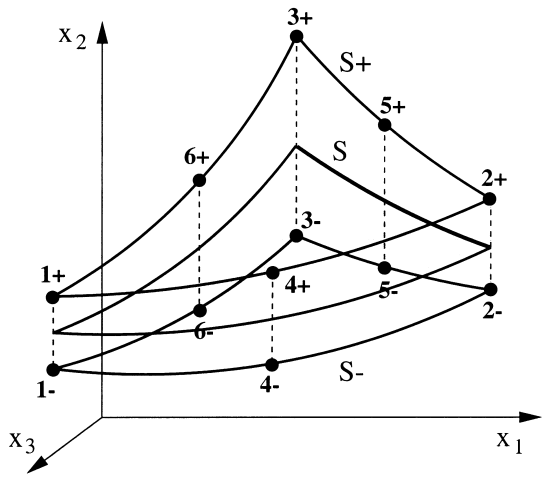

Fig. 9. Geometry of cohesive element. The surfaces S^- and S^+ coincide in the reference configuration of the solid.

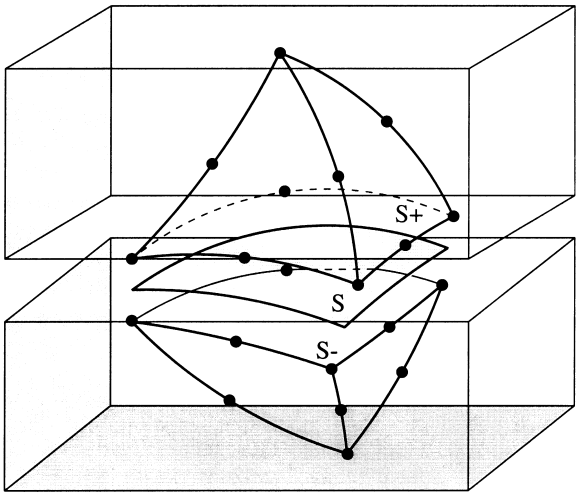

Fig. 10. 3D assembling of a 12-nodes triangular cohesive element with 10-nodes tetrahedra.

cohesive law as a mixed boundary condition, relating tractions to displacements at boundaries or interfaces (Hillerborg et al., 1976; Carpinteri, 1986; Needleman, 1987, 1990a, b, 1992; Planas et al., 1994; Tvergaard and Hutchinson, 1993, 1996a, b). Here, by contradistinction, we follow Willam (1989), Ortiz and Suresh (1993) and Xu and Needleman (1994), and directly embed the cohesive law into surface-like finite elements, leading to the formulation of so-called 'cohesive' elements. In addition, we follow Camacho and Ortiz (1996) and adaptively create new surface as required by the cohesive model by duplicating nodes along previously coherent element boundaries. The introduction of cohesive surfaces may result in drastic changes in the topology of the model (Pandolfi and Ortiz, 1999). The nodes are subsequently released in accordance with a tension-shear cohesive law.

The geometry of the cohesive elements considered here is shown in Fig. 9. The element consists of two six-node triangles endowed with quadratic displacement interpolation. Fig. 10 also demonstrates the compatibility between the cohesive elements and ten-node volume elements. Inserting the displacement interpolation into the virtual work expression (7) leads to a system of semi-discrete equations of motion of the form:

$$\mathbf{M}\ddot{\mathbf{x}} + \mathbf{f}^{\text{int}}(\mathbf{x}) = \mathbf{f}^{\text{ext}}(t) \tag{22}$$

where $\mathbf{x}$ is the array of nodal coordinates, $\mathbf{M}$ is the mass matrix, $\mathbf{f}^{\text{ext}}$ is the external force array, and $\mathbf{f}^{\text{int}}$ is the internal force array. In calculations we use the second-order accurate central difference algorithm to discretize (22) in time (Belytschko, 1983; Hughes, 1983, 1987). Despite the fact that the time step is bounded by stability (Hughes, 1983), explicit integration is particularly attractive in three-dimensional calculations, where implicit schemes lead to system matrices which often exceed the available in-core storage capacity. Yet another advantage of explicit algorithms is that they are ideally suited for concurrent computing (Mathur et al., 1996).

4. Numerical tests and comparison with experiment

We have conducted detailed simulations of one of the drop-weight dynamic fracture tests described in the foregoing. We take this test as a convenient yet exacting validation problem for assessing the fidelity

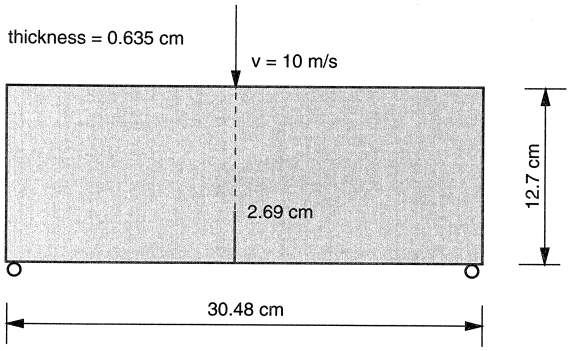

Fig. 11. Geometry of three-point bend test specimen.

of cohesive models in applications involving dynamic fracture. In particular, simulations of the drop-weight test effectively probe the ability of cohesive theories of fracture to track dynamically initiating and growing three-dimensional cracks in solids undergoing finite plastic deformations and heating. The assumed test configuration is shown in Fig. 11. A rectangular three-point bend specimen is subjected to

Bulk material **J2 Plasticity with power hardening, rate dependency, linear thermal softening**		**Cohesive Model**	
Mass density	$\rho = 7830\ kg/m^3$	Critical energy release rate	$G_c = 15000\ N/m$
Young's modulus	$E = 200\ GPa$	Maximum cohesive stress	$\sigma_c = 2\ GPa$
Poisson's ratio	$\nu = 0.3$	Critical displacement	$\delta_c = 1.5 \times 10^{-5} m$
Initial yield stress	$\sigma_0 = 1\ GPa$	Weighting coefficient	$\beta = 0.866$
Reference plastic strain	$\varepsilon_0^p = 4.9 \times 10^{-6}$	Mode I static toughness	$K_{Ic} = 57.5\ MPa\ m^{0.5}$
Reference plastic strain rate	$\dot{\varepsilon}_0^p = 0.001/s$		
Rate sensitivity exponent	$m = 70$		
Hardening exponent	$n = 10$		
Heat capacity	$c_v = 448\ J/kg\ K$		
Melting temperature	$T_m = 1440^{\circ}C$		
Thermal exponent	$\alpha = 1$		
Taylor-Quinney coefficient	$\beta_{TQ} = 0.9$		

Fig. 12. Material parameters for C300 steel adopted in the numerical calculations. The material is assumed to obey J_2-plasticity with power-law hardening, rate dependency and linear thermal softening (e.g. Cuitiño and Ortiz, 1992; Marusich and Ortiz, 1995; Camacho and Ortiz, 1997). The temperature field is calculated locally assuming adiabatic conditions.

dynamic loading as imparted by a falling weight which strikes at the midsection of the specimen. The specimen has an initial precrack 2.54 cm deep within its midsection sharpened by fatigue, Fig. 11.

The effect of the falling weight is approximated by prescribing a constant velocity of 10 m/s at the point of contact. Because of the impulsive nature of the motion, the problem is ideally suited to explicit dynamics. In explicit calculations a cohesive law of the form shown in Fig. 8(b) is preferable to a law of the Smith–Ferrante type, Fig. 8(a), as the initial elastic slope in the latter may place stringent restrictions on the stable time step for explicit integration. The material — brittle C300 steel — is assumed to obey J_2-plasticity with power-law hardening and rate dependency, as well as linear thermal softening. The temperature field is calculated locally assuming adiabatic conditions (e.g. Cuitiño and Ortiz, 1992; Marusich and Ortiz, 1995; Camacho and Ortiz, 1997). The volume elements are 10-node quadratic tetrahedra and the state variables are updated by recourse to the method of extension of Cuitiño and Ortiz (1992). In view of the brittleness of the C300 steel under consideration, the extent of shear lip formation may be expected to be small. Consequently, the crack surface may be approximated as remaining essentially planar and confined to the midsection of the specimen. In order to allow for dynamic crack growth, we tile the midsection of the specimen with cohesive elements such as described above. Fig. 12 collects the material parameters employed in the calculations. The constitutive material parameters have been obtained in-house, by means of Kolsky bar experiments performed on C300 steel specimens of the same batch and heat treatment as those used in the fracture experiments. The quasi-static fracture parameters (K_{IC}, G_C) have been established by using fracture specimens of the same geometry as in the dynamic tests loaded hydraulically in a three point bend configuration.

The computational meshes are shown in Figs. 13 and 14. The meshes are designed so as to be fine and nearly uniform on and in the vicinity of the crack plane, and to gradually coarsen away from the

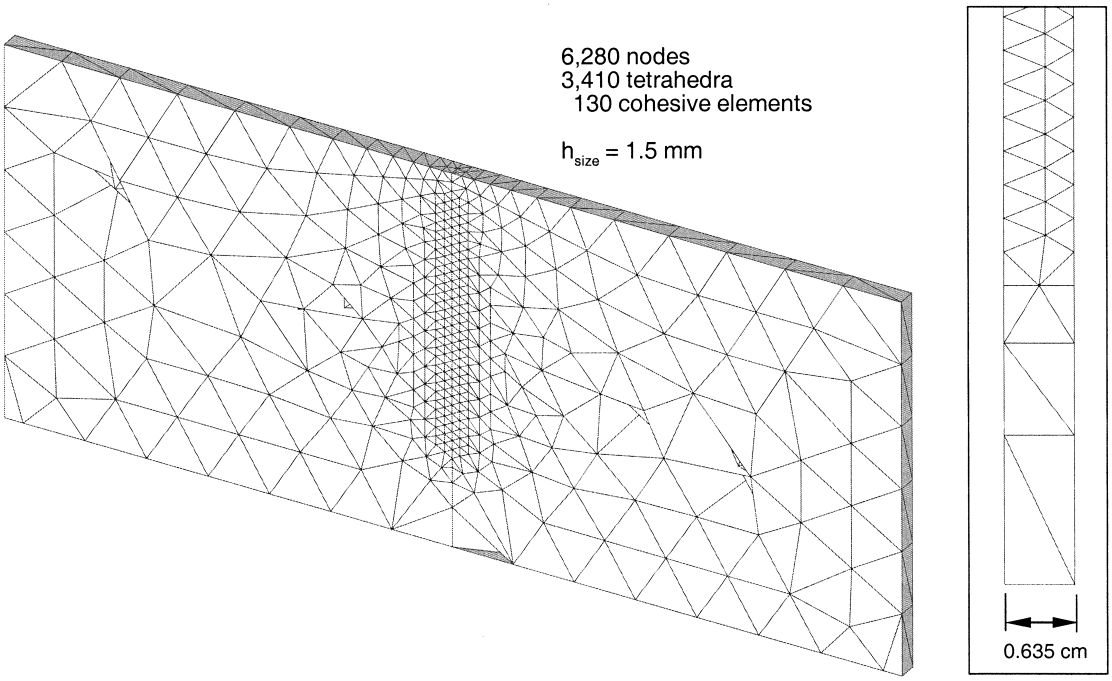

Fig. 13. Overall view and detail of the crack plane corresponding to a coarse finite element mesh comprising 6280 nodes, 3410 tetrahedra and 130 cohesive elements.

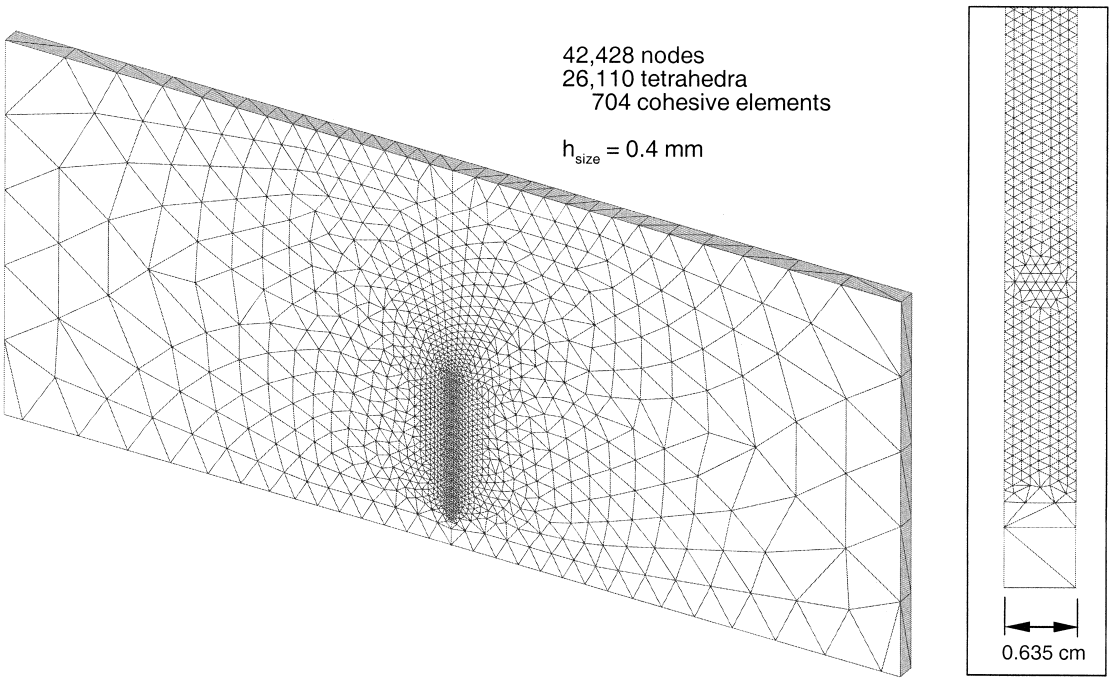

Fig. 14. Overall view and detail of the crack plane corresponding to a fine finite element mesh comprising 42,428 nodes, 26,110 tetrahedra and 704 cohesive elements.

crack plane up to a large uniform mesh size. All surfaces and the interior of the specimen are meshed automatically by an advancing front method (Radovitzky and Ortiz, 1998). In order to investigate the influence of mesh size, we have considered a coarse mesh, which contains 6280 nodes, 3410 tetrahedra and 130 cohesive elements; and a fine mesh comprising 42,428 nodes, 26,110 tetrahedra and 704 cohesive elements. The minimum mesh size in the fine mesh is 0.4 mm, which reasonably resolves the cohesive zone size. Based on this dimension and the elastic moduli, a stable time step for explicit

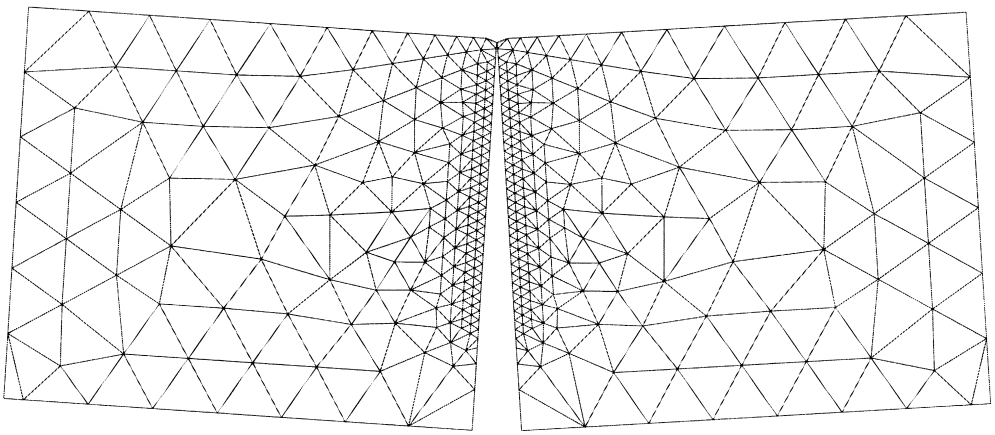

Fig. 15. Deformed geometry of the specimen after 2.4 ms.

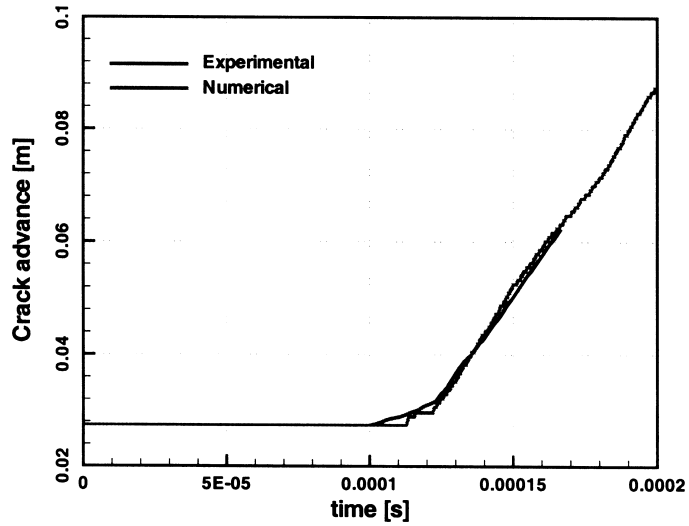

(a)

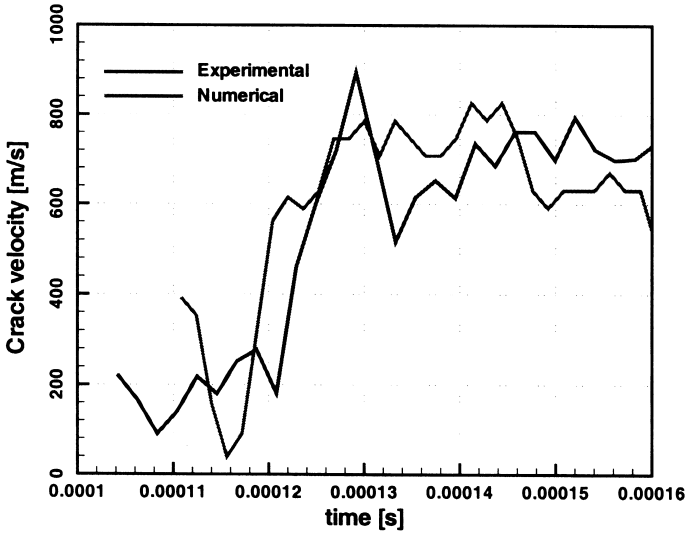

(b)

Fig. 16. (a) Experimental (black) and numerical (gray) crack tip trajectories. (b) Crack-tip velocity computed by a three-point numerical differentiation formula. Calculations done using coarse mesh of Fig. 13.

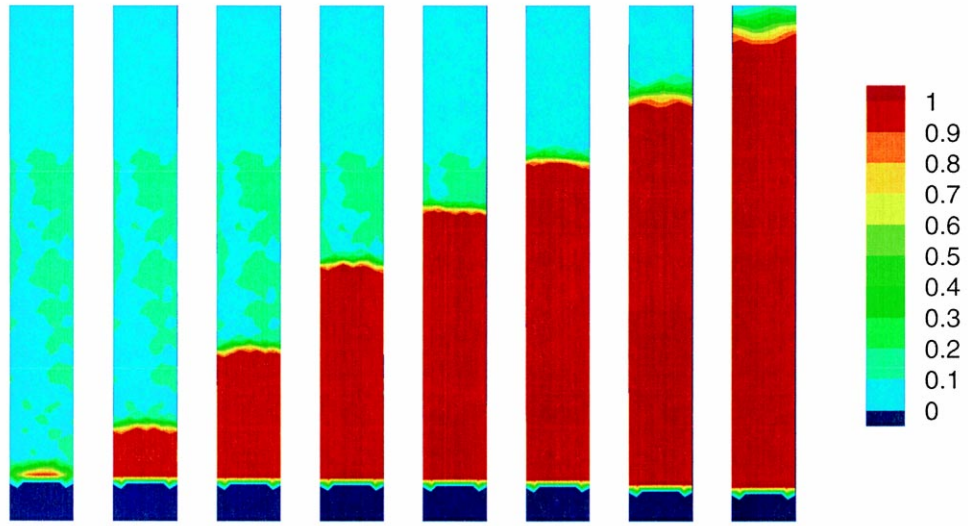

Fig. 17. Level contours of the damage variable D showing different stages of crack growth (Δt = 10 μs). Calculations done using fine mesh of Fig. 14.

integration may conservatively be estimated as Δt = 0.005 μs. The dynamic analysis starts at impact and its duration is 200 μs, or a total of 40,000 time steps.

The deformed mesh for the coarse model is shown to scale in Fig. 15 after the passage of 2.4 ms. At this time, the specimen is clearly split into two identical fragments. The finite rotations undergone by the specimen should be carefully noted, as they demonstrate the need to account for finite kinematics in the calculations. It is also interesting to note that the temperature rise is confined to a narrow zone

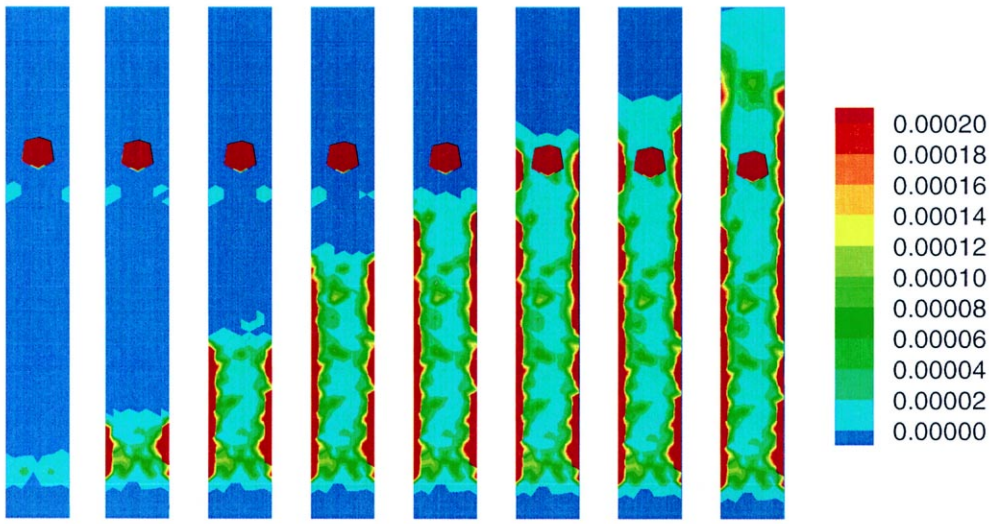

Fig. 18. Level contours of the equivalent plastic strain at different stages of crack growth (Δt = 10 μs), showing the development of shear lips near the lateral surfaces. Calculations done using fine mesh of Fig. 14.

surrounding the crack tip, and to the region of contact between the specimen and the impactor, where plastic deformations are large. Indeed, as the falling weight strikes the specimen, it deeply indents the top surface, with the result that as the crack approaches the surface it encounters material which has been prestressed plastically.

The ability of the cohesive elements to simulate the emergence of the crack through the upper surface of the specimen is noteworthy. As the crack approaches the surface, the ligament diminishes steadily and eventually becomes comparable in size with the plastic zone, at which point the small-scale yielding condition breaks down. The situation is further compounded by the fact that the region where the crack cuts through the top surface is plastically prestrained by the weight, a circumstance which influences the propagation of the crack. It is therefore noteworthy that a single description of the fracture behavior of the material, supplied by the cohesive model, effectively governs all phases of the growth of the crack, including crack-growth initiation, propagation, both in the interior of the specimen and at the specimen lateral surface, and the intersection of the crack and upper surface. By way of sharp contrast, within the conventional fracture mechanics framework exemplified by the fracture criterion (1), each of these aspects of crack growth requires a different ad hoc criterion tuned to the prevailing conditions of deformation, which greatly increases the degree of empiricism of the formulation.

The numerical and experimental trajectory and speed of the central point of the crack front are plotted in Fig. 16. It is evident from Fig. 16(a) that the cohesive model matches the point of crack-growth initiation and the subsequent trajectory of the crack remarkably well. The velocity history of the crack front as computed by a three-point numerical differentiation formula is shown in Fig. 16(b). The agreement between simulation and observation is as good as may be expected when derivatives of primitive quantities are computed. Again, it should be carefully noted that the velocity of the crack tip is an *outcome* of the calculation and is not in any way built into the model a priori.

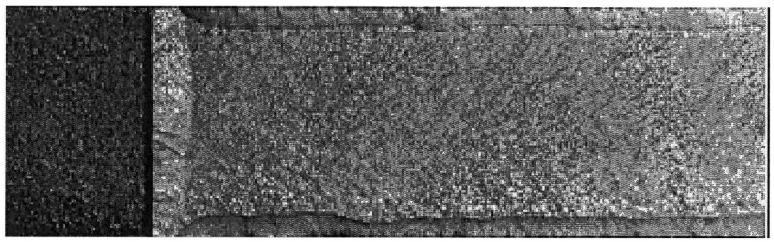

(a)

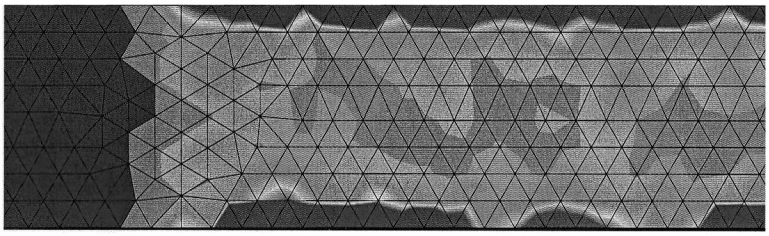

(b)

Fig. 19. (a) Experimental fracture surface. (b) Level contours of equivalent plastic strain 0.2 ms after impact. Calculations done using fine mesh of Fig. 14.

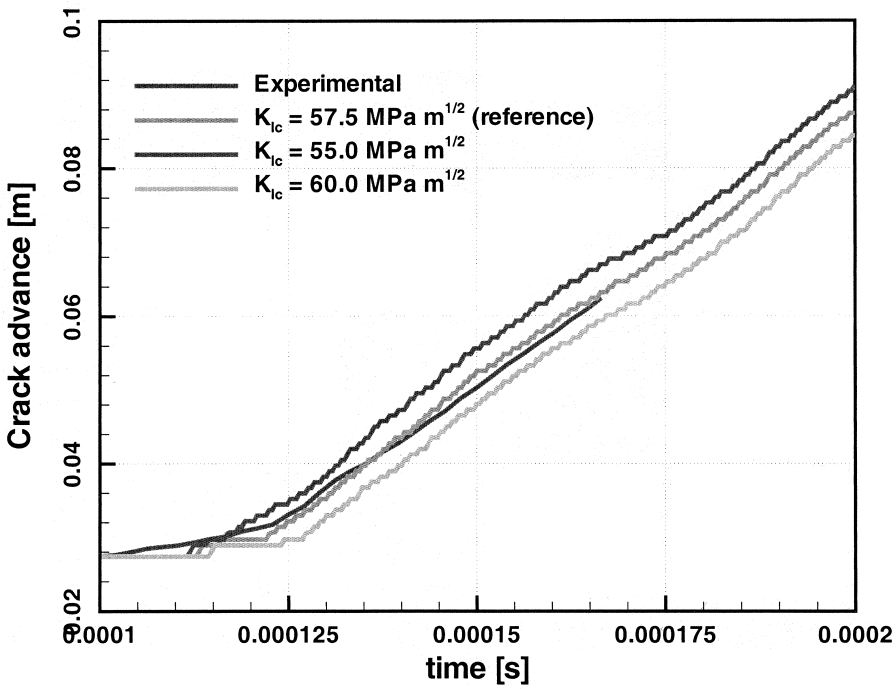

Fig. 20. Sensitivity of the crack tip trajectory to variations in the fracture toughness K_{Ic}. Calculations done using coarse mesh of Fig. 13.

Details of the crack growth process are shown in Figs 17–19. Fig. 17 depicts contours of the damage variable D, Eq. (20), at different stages of growth. A value of $D = 0$ denotes the absence of cracking, whereas the limiting value of $D = 1$ denotes a fully formed crack. The narrow transition zone between these two limiting values may be regarded as a smeared crack tip, or cohesive zone. It is observed in Fig. 17 that the crack front develops a small curvature as it propagates and it lags behind somewhat near the free surface as a consequence of enhanced plastic activity in that region (tunneling). This enhanced plastic activity is clearly evident in Fig. 18, which shows the contours of the equivalent plastic strain. A direct comparison of the computed plastic activity and the experimentally observed plastic surface is also shown in Fig. 19. As expected the plastic zone is markedly larger near the free surface, Fig. 19(b), as a consequence of the attendant loss of constraint and the emergence of shear lips, Fig. 19(a). The good agreement between the observed size of the shear lips and the computed zone of enhanced plastic activity near the surface is noteworthy.

While these features are relatively weak in C300 steel, as befits the brittleness of the material, they nevertheless serve to illustrate the point that the shielding effect of plasticity and the attendant retardation of the crack tip are indeed predicted by the simulations. Furthermore, it should be noted that such effects are not built into the fracture criterion a priori, but rather follow naturally from the explicit consideration of plasticity over multiple length scales, including the scale of the near tip fields.

A sensitivity analysis of the crack-tip trajectory to the fracture toughness K_{Ic}, the cohesive strength σ_c, and the ratio $\beta = K_{IIc}/K_{Ic}$ is shown in Figs. 20–22. As may be seen from Fig. 20, the main effect of an increase (decrease) in K_{Ic} is to retard (anticipate) the crack-growth initiation time. Interestingly, the effect of a variation in K_{Ic} on the crack propagation velocity is negligible by comparison, Fig. 20. Similarly, an increase (decrease) in the cohesive strength σ_c retards (anticipates) the crack-growth

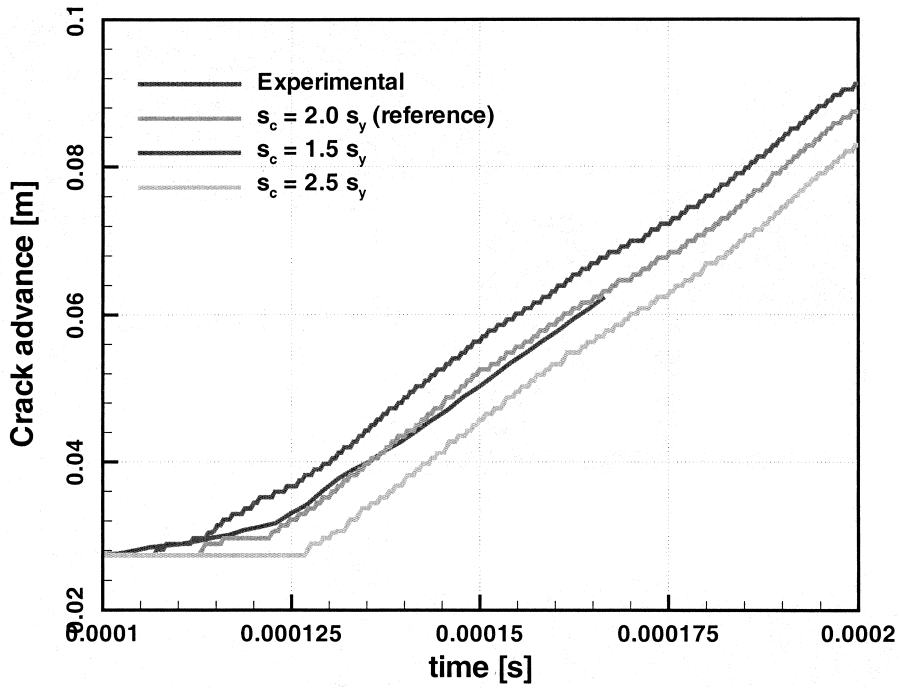

Fig. 21. Sensitivity of the crack tip trajectory to variations in the cohesive strength σ_c. Calculations done using coarse mesh of Fig. 13.

initiation time and has little or no effect on the crack propagation velocity, Fig. 21. Finally, we have investigated the sensitivity of the crack trajectory to the parameter β appearing in the definition of the effective opening displacement, Eq. (12). This parameter may be interpreted as the ratio K_{IIc}/K_{Ic} of mode II to mode I toughness. As expected from the primarily mode I character of the crack growth in the drop-weight test, the ratio β has little or no effect on the crack trajectory, Fig. 22. This fact can be explained observing that the brittle nature of C300 steel does not allow for the development of large shear lips, i.e. regions where decohesion has taken place by a primarily 3-D shear failure mechanism.

5. Summary and conclusions

We have taken the dynamic drop-weight test as a convenient basis for assessing the fidelity and predictive ability of cohesive models of fracture in applications involving dynamic crack growth. In an experimental phase of the study, CGS has been used to study dynamic fracture in C300 maraging steel. The specimens were subjected to three-point bend impact loading under a drop weight tower. High-speed photographs of the CGS interferograms were analyzed to determine the crack tip location and velocity and dynamic stress intensity factor as a function of time. Post-mortem examination of the specimens revealed the fractography of the fracture surfaces, including the development of shear lips. In a parallel numerical phase of the study, fracture has been modelled by recourse to an irreversible cohesive law embedded into cohesive elements. These cohesive elements govern all aspects of the separation and closure of the incipient cracks. The cohesive behavior of the material is assumed to be rate independent and, consequently, all rate effects predicted by the calculations are due to inertia and

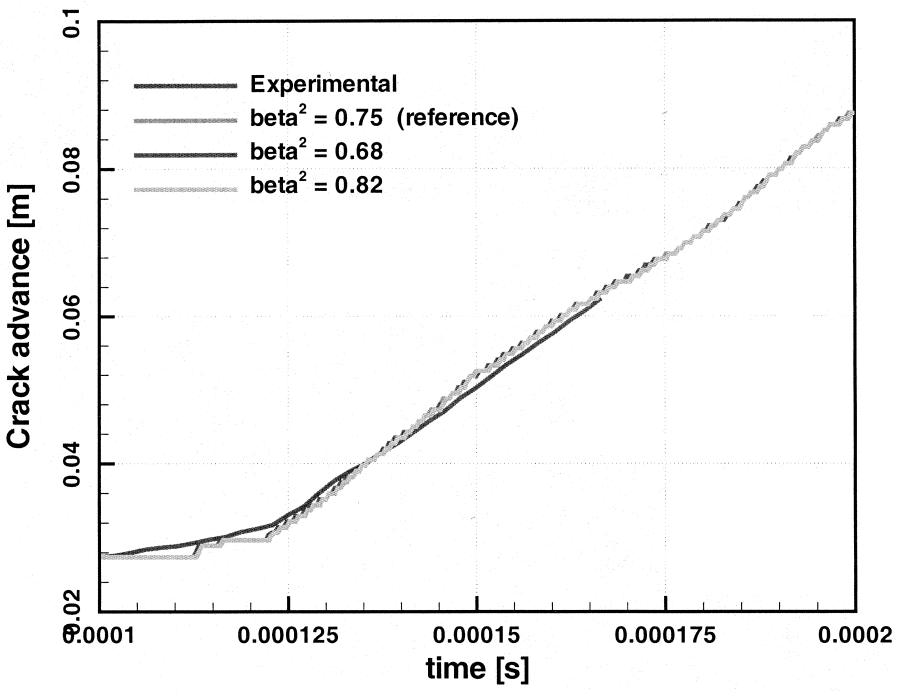

Fig. 22. Sensitivity of the crack tip trajectory to variations in the ratio $\beta = K_{IIc}/K_{Ic}$. Calculations done using coarse mesh of Fig. 13.

the rate dependency in plastic deformation. The finite element model is three dimensional and consists of quadratic ten-noded tetrahedra. The numerical models were calibrated by means of experimentally obtained constitutive and cohesive law parameters.

The numerical simulations have proven highly predictive of a number of observed features, including: the crack growth initiation time; the trajectory of the propagating crack tip; and the formation of shear lips near the lateral surfaces. These features follow naturally from a single description of the fracture properties of the material, supplied by the cohesive law, and are not built in piecemeal into the model. By separately accounting for plasticity, inertia and thermal effects, the description of the fracture behavior may focus sharply on the separation processes responsible for the creation of new surface, which considerably cuts down on the level of phenomenology of the theory. In this particular sense, the fracture model and the bulk constitutive relations constitute truly independent mechanical postulates. In particular, the applicability of the theory is not restricted by the type of bulk behavior, the geometry of the specimen and loading, the size of the plastic region or the presence or absence of inertia.

It should also be noted that the use of cohesive theories in calculations relies strongly on the ability to resolve multiple length scales simultaneously. Thus, Camacho and Ortiz (1996) have also shown that mesh-size independent results are obtained when the mesh adequately resolves the cohesive zone, which tends to be small in typical materials. Recent advances in automatic meshing, mesh adaption and computer hardware have contributed to making the type of multiscale analysis called for by cohesive models increasingly feasible. In this particular sense, cohesive models of fracture partake of the present emphasis on physics-based multiscale analysis of materials, an emphasis which may only be expected to be affirmed in the future.

Acknowledgements

The support of the Office of Naval Research through grant N00014-95-1-0453 is gratefully acknowledged.

References

Angelino, G.C., 1978. Influence of the geometry on unstable crack extension on determination of dynamic fracture mechanics parameters. In Testing, A. S. and Materials, editors, Fast Fracture and Crack Arrest, volume ASTM STP 627, pp. 392–407.

Atluri, S.N., Nishioka, T., 1983. Path-independent integrals, energy release rates and general solutions of near tip fields in mixed mode dynamic fracture mechanics. Engineering Fracture Mechanics 28, 1–22.

Barrenblatt, G.I., 1962. The mathematical theory of equilibrium of cracks in brittle fracture. Advances in Applied Mechanics 7, 55–129.

Beinert, J., Kalthoff, J.F., 1981. Experimental determination of dynamic stress intensity factors by shadow patterns. In: Sih, G. (Ed.), Mechanics of Fracture, vol. VII. Sijthoff and Noordhoff, pp. 281–330.

Beltz, G.E., Rice, J.R. 1991. Dislocation nucleation versus cleavage decohesion at crack tips. In: Lowe, T.C., Rollett, A.D., Follansbee, P.S., Daehn, G.S. (Eds.), Modeling the Deformation of Crystalline Solids: Physical Theory, Application and Experimental Comparisons. Warrendale, PA, pp. 457–480 TSM-AIME.

Belytschko, T. 1983. An overview of semidiscretization and time integration procedures. In: Belytschko, T., Hughes, T.J.R. (Eds.), Computational Methods for Transient Analysis. North-Holland, pp. 1–65.

Bilek, Z., 1980. Some comments on dynamic crack propagation in a high strength steel. In Testing, A. S. and Materials, editors, Crack Arrest Methodology and Applications, volume ASTM STP 711, pp. 240–247.

Bradley, W.B., Kobayashi, A.S., 1970. An investigation of propagating cracks by dynamic photoelasticity. Experimental Mechanics 10, 106–113.

Brickstad, B., 1983. A fem analysis of crack arrest experiments. International Journal of Fracture 21, 177–194.

Camacho, G.T., Ortiz, M., 1996. Computational modelling of impact damage in brittle materials. International Journal of Solids and Structures 33 (2022), 2899–2938.

Camacho, G.T., Ortiz, M., 1997. Adaptive Lagrangian modelling of ballistic penetration of metallic targets. Computer Methods in Applied Mechanics and Engineering 142, 269–301.

Carpinteri, A., 1986. Mechanical Damage and Crack Growth in Concrete. Martinus Nijhoff, Dordrecht, The Netherlands.

Chen, W.N., Ravichandran, G., 1994. Dynamic compressive behavior of ceramics under lateral confinement. Journal de Physique IV 4, 177–182.

Chen, W.N., Ravichandran, G., 1996. Static and dynamic compressive behavior of aluminum nitride under moderate confinement. Journal of the American Ceramic Society 79, 579–584.

Chona, R., Irwin, G.R., Sanford, R.J., 1983. Influence of specimen size and shape on the singularity dominated zone. In: Lewis, J.C., Sines, G. (Ed.). Fracture Mechanics: 14th Symposium Volume I. Theory and Analysis, ASTM STP 791, pp. I/3–I/23.

Chona, R., Sanford, R.J., 1988. Analyzing crack tip isochromatic fringe patterns. In VI International Congress of Experimental Mechanics, pp. 751–760.

Cuitiño, A.M., Ortiz, M., 1992. A material-independent method for extending stress update algorithms from small-strain plasticity to finite plasticity with multiplicative kinematics. Engineering Computations 9, 437–451.

Dally, J.W., 1979. Dynamic photoelastic studies of fracture. Experimental Mechanics 19, 349–361.

Dally, J.W., Fourney, W.G., Irwin, G.R., 1985. On the uniqueness of k_{ID}–$\dot{a}$ relation. International Journal of Fracture 27, 159–168.

De-Andrés, A., Pérez, J.L., Ortiz, M., 1998. Elastoplastic finite element analysis of three-dimensional fatigue crack growth in aluminum shafts subjected to axial loading. International Journal of Solids and Structures. In press.

Dugdale, D.S., 1960. Yielding of steel sheets containing slits. Journal of the Mechanics and Physics of Solids 8, 100–104.

Freund, L.B., 1972. Crack propagation in an elastic solid subjected to general loading-i constant rate extension. Journal of the Mechanics and Physics of Solids 20, 129–140.

Freund, L.B., 1990. Dynamic Fracture Mechanics. Cambridge University Press, Cambridge.

Freund, L.B., Douglas, A.S., 1982. The influence of inertia on elastic-plastic antiplane-shear crack growth. Journal of the Mechanics and Physics of Solids 30, 59–74.

Freund, L.B., Hutchinson, J.W., 1985. High strain-rate crack growth in rate-dependent plastic solids. Journal of the Mechanics and Physics of Solids 33, 169–191.

Freund, L.B., Hutchinson, J.W., Lam, P.S., 1986. Analysis of high strain rate elastic-plastic crack growth. Engineering Fracture Mechanics 23, 119–129.

Freund, L.B., Rosakis, A.J., 1992. The structure of the near tip field solution during transient elastodynamic crack growth. Journal of the Mechanics and Physics of Solids 40, 699–719.

Goldsmith, W., Katsamanis, F., 1979. Fracture of notched polymeric beams due to central impact. Experimental Mechanics 18, 235–244.

Grady, D.E., Benson, D.A., 1983. Fragmentation of metal rings by electromagnetic loading. Experimental Mechanics 23, 393–400.

Hillerborg, A., Modeer, M., Petersson, P.E., Needleman, A., 1976. Analysis of crack formation and crack growth in concrete by means of fracture mechanics and finite elements. Cement Concrete Resarch 6, 773–782.

Hughes, T.J.R. 1983. Analysis of transient algorithms with particular reference to stability behavior. In: Belytschko, T., Hughes, T.J.R. (Eds.), Computational Methods for Transient Analysis. North-Holland, pp. 67–155.

Hughes, T.J.R., 1987. The Finite Element Method: Linear Static and Dynamic Finite Element Analysis. Prentice-Hall, Englewood Cliffs, NJ.

Irwin, G.R., 1958. In Proceedings of SESA, volume 16, pp. 93–96.

Irwin, G.R., Dally, J.W., Kobayashi, T., Fourney, W.L., Etheridge, M.J., Rossmanith, H.P., 1979. On the determination of the $\dot{a}$-K relationship for birefringent polymers. Experimental Mechanics 19, pp. 121–128.

Kalthoff, J.F., 1985. On the measurement of dynamic fracture toughness — a review of recent work. International Journal of Fracture 27, 277–298.

Kalthoff, J.F., Beinert, J., Winkler, S., 1978. Influence of dynamic effects on crack arrest. Technical report, Institut fur Festkorpermechanik.

Kalthoff, J.F., Winkler, S., Beinert, J., 1976. Dynamic stress intensity factors for arresting cracks in DCB specimens. International Journal of Fracture 12, 317–319.

Kanazawa, T., Machida, S., Teramoto, T., Yoshinari, H., 1981. Study on fast fracture and crack arrest. Experimental Mechanics 21 pp. 78–88.

Katsamanis, F., Raftopoulos, D., Theocaris, P.S., 1977. Static and dynamic stress intensity factors by the method of transmitted caustics. Journal of Engineering Materials and Technology 99, 105–109.

Knauss, W.G., Ravi-Chandar, K., 1985. Some basic problems in stress wave dominated fracture. International Journal of Fracture 27, 127–143.

Kobayashi, A.S., 1978. Investigation of Transient Effects for Dynamically Initiating and Growing Cracks Under Stress Wave Loading Conditions. University Press, Virginia, pp. 481–496.

Kobayashi, T., Dally, J.W., 1980. Dynamic photoelastic determination of the $\dot{a}$-K relation for 4340 alloy steel. In: Hahn, G.T., Kanninen, M.F. (Eds.), Crack Arrest Methodology and Applications, vol. ASTM STP 711, pp. 189–210.

Krishnaswamy, S., Rosakis, A.J., 1990. On the extent of dominance of asymptotic elastodynamic crack tip fields: Part I — an experimental study using bifocal caustics. Journal of Applied Mechanics 58, 87–94.

Krishnaswamy, S., Rosakis, A.J., Ravichandran, G., 1991. On the extent of dominance of asymptotic elastodynamic crack tip fields: Part II — numerical investigation of three dimensional and transient effects. Journal of Applied Mechanics 58, 95–103.

Krishnaswamy, S., Tippur, H.V., Rosakis, A.J., 1992. Measurement of transient crack tip deformation fields using the method of cgs. Journal of the Mechanics and Physics of Solids 40, 339–372.

Lam, P.S., Freund, L.B., 1984. Analysis of dynamic growth of a tensile crack in an elastic–plastic material. Journal of the Mechanics and Physics of Solids 33, 153–167.

Liu, C., Rosakis, A.J., Freund, L.B., 1993. The interpretation of optical caustics in the presence of non-uniform crack tip motion histories: a study based on a higher order transient crack tip expansion. International Journal of Solids and Structures 30, 875–897.

Lubliner, J., 1972. On the thermodynamic foundations of non-linear solid mechanics. International Journal of Non-Linear Mechanics 7, 237–254.

Lubliner, J., 1973. On the structure of the rate equations of materials with internal variables. Acta Mechanica 17, 109–119.

Marsden, J.E., Hughes, T.J.R., 1983. Mathematical Foundations of Elasticity. Prentice-Hall, Englewood Cliffs, NJ.

Marusich, T.D., Ortiz, M., 1995. Modelling and simulation of high-speed machining. International Journal for Numerical Methods in Engineering 38, 3675–3694.

Mathur, K.K., Needleman, A., Tvergaard, V., 1996. Three dimensional analysis of dynamic ductile crack growth in a thin plate. Journal of the Mechanics and Physics of Solids 44, 439–464.

McClintock, F., Irwin, G.R., 1964. Fracture toughness testing and applications, volume ASTM STP 381, p. 95.

Needleman, A., 1987. A continuum model for void nucleation by inclusion debonding. Journal of Applied Mechanics 54, 525–531.

Needleman, A., 1990a. An analysis of decohesion along an imperfect interface. International Journal of Fracture 42, 21–40.

Needleman, A., 1990b. An analysis of tensile decohesion along an interface. Journal of the Mechanics and Physics of Solids 38 (3), 289–324.

Needleman, A., 1992. Micromechanical modeling of interfacial decohesion. Ultramicroscopy 40, 203–214.

Ortiz, M., 1988. Microcrack coalescence and macroscopic crack growth initiation in brittle solids. International Journal of Solids and Structures 24, 231–250.

Ortiz, M., 1996. Computational micromechanics. Computational Mechanics 18, 321–338.
Ortiz, M., Pandolfi, A., 1999. A class of cohesive elements for the simulation of three-dimensional crack propagation. International Journal for Numerical Methods in Engineering 44, 1267–1282.
Ortiz, M., Suresh, S., 1993. Statistical properties of residual stresses and intergranular fracture in ceramic materials. Journal of Applied Mechanics 60, 77–84.
Owen, D.M., Zhuang, S., Rosakis, A.J., Ravichandran, G., 1998. Experimental determination of dynamic crack initiation and propagation fracture toughness in thin aluminum sheets. International Journal of Fracture 90, 153–174.
Pandolfi, A., Krysl, P., Ortiz, M., 1999. Finite element simulation of ring expansion and fragmentation: the capturing of length and time scales through cohesive models of fracture. International Journal of Fracture. In press.
Pandolfi, A., Ortiz, M., 1999. Solid modeling aspects of three-dimensional fragmentation. Engineering with Computers 14, 287–308.
Planas, J., Elices, M., Guinea, G.V. 1994. Cohesive cracks as a solution of a class of nonlocal problems. In: Bazant, Z.P. (Ed.), Fracture and Damage in Quasibrittle Structures. Experiment, Modelling and Computer Analysis. E & FN SPON.
Radovitzky, R., Ortiz, M., 1998. Tetrahedral mesh generation based on node insertion in crystal lattice arrangements and advancing-front-Delaunay triangulation. Computer Methods in Applied Mechanics and Engineering. In press.
Ravi-Chandar, K., Knauss, W.G., 1983. Dynamic crack tip stresses under stress wave loading — a comparison of theory and experiment. International Journal of Fracture 20, 209–222.
Ravi-Chandar, K., Knauss, W.G., 1984a. An experimental investigation into dynamic fracture, Part 1. Crack initiation and arrest. International Journal of Fracture 25 (4), 247–262.
Ravi-Chandar, K., Knauss, W.G., 1984b. An experimental investigation into dynamic fracture, Part 2. Microstructural aspects. International Journal of Fracture 26 (1), 65–80.
Ravi-Chandar, K., Knauss, W.G., 1984c. An experimental investigation into dynamic fracture, Part 3. On steady state crack propagation and crack branching. International Journal of Fracture 26 (2), 141–154.
Ravi-Chandar, K., Knauss, W.G., 1984d. An experimental investigation into dynamic fracture, Part 4. On the interaction of stress waves with propagating cracks. International Journal of Fracture 26 (3), 189–200.
Rice, J.R. 1968. Mathematical analysis in the mechanics of fracture. In: Liebowitz, H. (Ed.), Fracture. Academic Press, pp. 191–311.
Rice, J.R., 1992. Dislocation nucleation from a crack tip: an analysis based on the Peierls concept. Journal of the Mechanics and Physics of Solids 40, 235–271.
Rosakis, A.J., 1980. Analysis of the optical method of caustics for dynamic crack propagation. Engineering Fracture Mechanics 13, 331–347.
Rosakis, A.J. 1993. Two optical techniques sensitive to gradients of optical path difference: the method of caustics and the coherent gradient sensor (CGS). In: Epstein, J. (Ed.), Experimental Techniques in Fracture. VCH, New York, pp. 327–425.
Rosakis, A.J., Duffy, J., Freund, L.B., 1984. The determination of dynamic fracture toughness of aisi 4340 steel by the shadow spot method. Journal of the Mechanics and Physics of Solids 32, 443–460.
Rosakis, A.J., Liu, C., Freund, L.B., 1991. A note on the asymptotic stress field of a non-uniformly propagating dynamic crack. International Journal of Fracture 50, R39–R45.
Rosakis, A.J., Ravi-Chandar, K., 1986. On the crack tip stress state: An experimental evaluation of three dimensional effects. International Journal of Solids and Structures 22, 121–134.
Rosakis, A.J., Zehnder, A.T., 1985. On the dynamic fracture of structural metals. International Journal of Fracture 27, 169–186.
Rosakis, A.J., Zehnder, A.T., Narasimhan, R., 1988. Reflection and their application to elastic-plastic and dynamic fracture mechanics. Optical Engineering 27, 596–610.
Rose, J.H., Ferrante, J., Smith, J.R., 1981. Universal binding energy curves for metals and bimetallic interfaces. Physical Review Letters 47 (9), 675–678.
Sanford, R.J., Chona, R., 1984. Photoelastic calibration of the short-bar chevron notched specimen. In: Underwood, J.H., Freiman, S.W., Baratta, F.I. (Eds.), Chevron Notched Specimens: Testing and Stress Analysis, vol. ASTM STP 855, pp. 81–97.
Sanford, R.J., Dally, J.W., 1979. A general method for determining mixed mode stress intensity factors from isochromatic fringe patterns. Engineering Fracture Mechanics 11, 621–633.
Shukla, A., Chona, R. 1988. The stress field surrounding a rapidly propagating curving crack. In: Read, D.T., Reed, R.P. (Eds.), Fracture Mechanics, 18th Symposium, volume ASTM STP 945, pp. 86–99.
Theocaris, P.S., 1978. Dynamic propagation and arrest measurements by the method of caustics on overlapping skew-parallel cracks. International Journal of Solids and Structures 14, 639–653.
Tippur, H.V., Krishnaswamy, S., Rosakis, A.J., 1990. Coherent gradient sensor for crack tip deformation measurements: analysis and experimental results. International Journal of Fracture 48, 193–204.
Tippur, H.V., Krishnaswamy, S., Rosakis, A.J., 1991. Optical mapping of crack tip deformations using the method of transmission and reflection coherent gradient sensing: a study of crack tip k-dominance. International Journal of Fracture 52, 91–117.

Tvergaard, V., Hutchinson, J.W., 1993. The influence of plasticity on mixed-mode interface toughness. Journal of the Mechanics and Physics of Solids 41, 1119–1135.

Tvergaard, V., Hutchinson, J.W., 1996a. Effect of strain dependent cohesive zone model on predictions of interface crack growth. Journal de Physique IV 6, 165–172.

Tvergaard, V., Hutchinson, J.W., 1996b. Effect of strain dependent cohesive zone model on predictions of crack growth resistance. International Journal of Solids and Structures 33, 3297–3308.

Willam, K. 1989. Simulation issues of distributed and localized failure computations. In: Mazars, J., Bazant, Z.P. (Eds.), Cracking and Damage. Elsevier, New York, pp. 363–378.

Xu, X.P., Needleman, A., 1993. Void nucleation by inclusion debonding in a crystal matrix. Modelling and Simulation in Materials Science and Engineering 1, 111–132.

Xu, X.P., Needleman, A., 1994. Numerical simulations of fast crack growth in brittle solids. Journal of the Mechanics and Physics of Solids 42, 1397–1434.

Xu, X.P., Needleman, A., 1995. Numerical simulations of dynamic interfacial crack growth allowing for crack growth away from the bond line. International Journal of Fracture 74, 253–275.

Xu, X.P., Needleman, A., 1996. Numerical simulations of dynamic crack growth along an interface. International Journal of Fracture 74, 289–324.

Zehnder, A.T., Rosakis, A.J., 1986. A note on the measurement of K and J under small scale yielding conditions using the method of caustics. International Journal of Fracture 30, R43–R48.

Zehnder, A.T., Rosakis, A.J., 1990. Dynamic fracture initiation and propagation in 4340 steel under impact loading. International Journal of Fracture 43, 271–285.